nature materials

ARTICLES

PUBLISHED ONLINE: 15 JUNE 2015 | DOI: 10.1038/NMAT4278

The effect of mechanical twisting on oxygen ionic transport in solid-state energy conversion membranes

Yanuo Shi, Alexander Hansen Bork, Sebastian Schweiger and Jennifer Lilia Marguerite Rupp*

Understanding 'electro–chemo–mechanics' in oxygen ion conducting membranes represents a foundational step towards new energy devices such as micro fuel cells and oxygen or fuel separation membranes. For ionic transport in macro crystalline electrolytes, doping is conventionally used to affect oxygen ionic association/migration energies. Recently, tuning ionic transport in films through lattice strain conveyed by substrates or heterostructures has generated much interest. However, reliable manipulation of strain states to twist the ionic conduction in real micro energy devices remains intractable. Here, we demonstrate that the oxygen ionic conductivity clearly correlates with the compressive strain energy acting on the near order of the electrolyte lattices by comparing thin-film ceria-based membrane devices against substrate-supported flat structures. It is possible to capitalize on this phenomenon with a smart choice of strain patterns achieved through microelectrode design. We highlight the importance of electro–chemo–mechanics in the electrolyte material for the next generation of solid-state energy conversion microdevices.

The increased electrochemical conversion efficiency and reduced scale that thin-film structures bring to microfabricated solid-oxide fuel cells[1–4] and thin-film solid-state batteries[5] or performance enhancements in resistive random access memories[6,7] are often compromised by lowered transport kinetics at reduced operation temperatures. At the low deposition and operation temperatures required to ensure compatibility with today's silicon microsystem technology, oxide films remain in 'metastable states' with lattice strain that is expected to affect local order and therefore the transport properties of the conducting species[8–10]. In addition, free-standing oxide film membranes on silicon structures are subjected to additional mechanical deformations that may alter charge transport and electrochemical device performances[11,12]. For example, micro solid-oxide fuel performance varies in the range of 26–1,037 $\mathrm{mW\,cm^{-2}}$ at 500 °C and open circuit voltage, and so far there is no satisfactory explanation for these large variations[1,3]. Additionally, standard doped zirconia and ceria ionic conductor films reveal a high variability in ionic conductivity depending on processing[8,9] but this cannot be explained solely by nanoscopical changes in grain-to-grain boundary ratios.

An alternative explanation may be the electro–chemo–mechanic[13] coupling, the link between ionic charge carrier transport ('electro'), chemical stoichiometry ('chemo'), and mechanical strain acting on lattice structure ('mechanic'). Very recently, electro–mechanic modulations of ionic conductivity by strained interfaces were reported for substrate-supported thin films, and chemo–mechanic non-stoichiometry changes under strain were discussed for film membranes under strain, although the electro–chemo–mechanic coupling has not yet been pursued experimentally for real microdevices.

The electro–mechanic modulations of ionic conductivity by straining oxide volumes are reported for substrate-supported single- or heterolayer films[14–19]. Here, the defect thermodynamics and kinetics are tuned by imposing compressive or tensile strain introduced by insulating monolayers on ionic conducting layers in a heterostructure[15]. Interfacial strain can alter the conductivity through changes in the hopping sites and frequencies due to variations of the enthalpies of oxygen-vacancy migration and association (see Supplementary Information 4). It was reported for zirconia-based heterolayers with 7% tensile strain that the conduction can be altered by up to eight orders of magnitude[20]. Even though these findings are debated, a change in conduction as high as 3 orders of magnitude for strained thin films was confirmed[8,14,18,21]. In contrast, compressive lattice strain is reported to reduce the ionic conductivity and increase the activation energy of ceria- and zirconia-based thin films[14,21–25]. Computation of the oxygen ionic migration enthalpy changes for strained ceria resulted in the recently reported strain-activated volume tensor model[22,23]. We confirmed experimentally the ability of the model to accurately describe the ionic transport–strain electro–mechanic interaction on the example of strained $\mathrm{Ce_{0.9}Gd_{0.1}O_{2-x}/Er_2O_3}$ heterolayer micro-dots[15]. In the literature most attention has been paid to modulating electro–mechanic interaction through strained interfaces of substrate-supported films, but their integration as free-standing membranes in micro electrochemical silicon-based devices has still to be undertaken. In essence, strain engineering has the potential to alter ionic transport in electrolytes by far more than classic solid-state doping, and requires attention.

Understanding chemo–mechanic interaction for free-standing ionic conducting oxide membranes under strain is a hot topic[8,14,21,26]. In numerous technologically relevant micro energy converters, an ionic conducting oxide thin film serves as a free-standing (electrolyte) membrane, for example, in micro solid-oxide fuel cells[1,2]. Here, fabrication of the device is achieved by free-etching the substrate area underneath an electrolyte film forming a strained and buckled ionic conducting membrane[27–29]. Very recently, the residual stress and buckling profiles of free-standing yttria-stabilized-zirconia membranes were investigated by optical microscopy[30,31] and interferometry[11,32]. Numeric simulations based on the Rayleigh–Ritz or von Karman methods were used to analyse the membrane stress patterns with respect to their thickness[11], buckling geometry[32], membrane aspect ratio[30], or

Electrochemical Materials, Department of Materials, ETH Zurich, CH-8093, Switzerland. *e-mail: jennifer.rupp@mat.ethz.ch

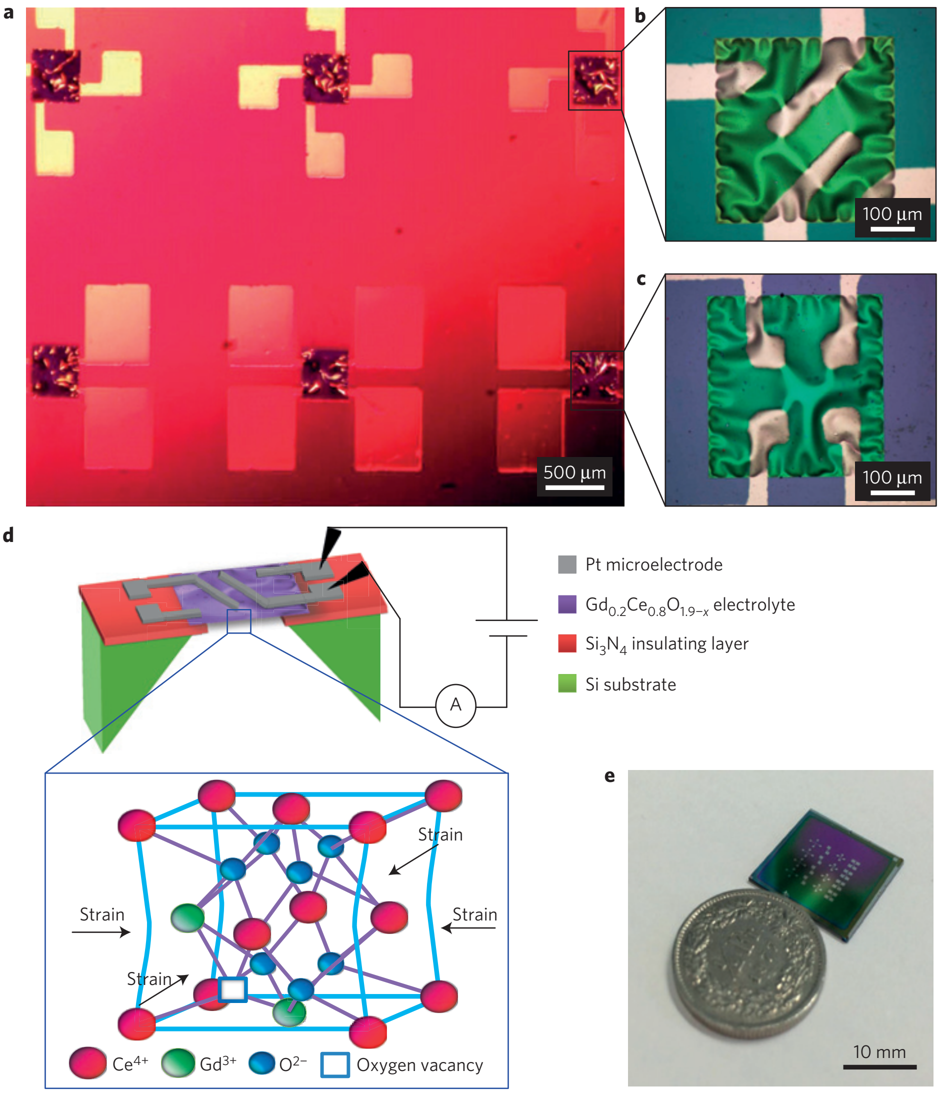

Figure 1 | Micro energy conversion membranes with different microelectrode patterns. Model systems to study electro–chemo–mechanics. **a**, Optical micrograph of free-standing buckled $Ce_{0.8}Gd_{0.2}O_{1.9-x}$ membranes with various designs of top platinum microelectrodes on a Si_3N_4/Si chip. **b**,**c**, Optical micrographs of two different Pt microelectrode designs and arrangements on free-standing $Ce_{0.2}Gd_{0.8}O_{1.9-x}$ thin-film membranes. **d**, Schematic of a free-standing electrochemical membrane device, for example, micro solid-oxide fuel cell, with an integrated model top electrode design for electric measurements with respect to biaxial 'net strains' (buckling). **e**, Image of the 15 × 15 mm Si_3N_4/Si chip with up to 16 $Ce_{0.2}Gd_{0.8}O_{1.9-x}$ thin-film membranes with varied microelectrode designs and local compressive strain patterns (compared with a Swiss 1 CHF coin).

film deposition temperature[31]. It is reported that mechanical compressive stress acting on ceria-based membranes can modify the specific volume and shift the point defect equilibrium[33–35]. Such chemical strain effects can influence the elastic modulus and the overall ionic vacancy concentration and formation[34,36]. There have been experimental efforts directed towards describing the buckling and its impact on membranes, but it remains unclear what effect these chemo–mechanics may have for the overall ionic conduction. New fundamentals on electro–chemo–mechanics may be the missing link, introducing strain as a new material parameter accessible for tuning ionic transport in metal oxide membranes in solid-state energy devices.

In the present work we explore the electro–chemo–mechanical coupling of $Ce_{0.8}Gd_{0.2}O_{1.9-x}$ films by assessing the relative oxygen ionic conductivity change for various compaction degrees in oxide lattice strain by the use of Pt microelectrodes with different geometries.

To demonstrate the role of strain on the conductivity characteristics, free-standing buckled membranes are compared with fully substrate-supported and flat $Ce_{0.8}Gd_{0.2}O_{1.9-x}$ electrolyte films for similar electrode patterns. Images of various Pt microelectrode geometries on free-standing buckled membranes of $Ce_{0.8}Gd_{0.2}O_{1.9-x}$ films, with a total membrane area size of 400 µm × 400 µm, on a Si chip are shown in close-ups of the Si chip (Fig. 1a–c). For all membranes, excellent electrode-to-oxide film adhesion properties are shown independent of the pattern geometry. The changes in the $Ce_{0.8}Gd_{0.2}O_{1.9-x}$ electrolyte films' buckling profiles are directly visible when comparing the different 4-point top Pt electrode geometries (Fig. 1b,c). We observe a maximum buckling of the $Ce_{0.8}Gd_{0.2}O_{1.9-x}$ film between the two inner electrodes of the asymmetric arrangement (Fig. 1b), and at the middle of the membrane for symmetric electrode placing (Fig. 1c). We show chip-level microfabrication and reproduction of the membrane strain patterns when comparing three membranes per row with similar electrode patterns (Fig. 1a–c). A schematic of a $Ce_{0.8}Gd_{0.2}O_{1.9-x}$ buckled membrane and the resulting biaxial compressive strain acting on its atomistic positions is shown in Fig. 1d. The *in situ* heated X-ray diffraction patterns of the $Ce_{0.8}Gd_{0.2}O_{1.9-x}$ films reveal

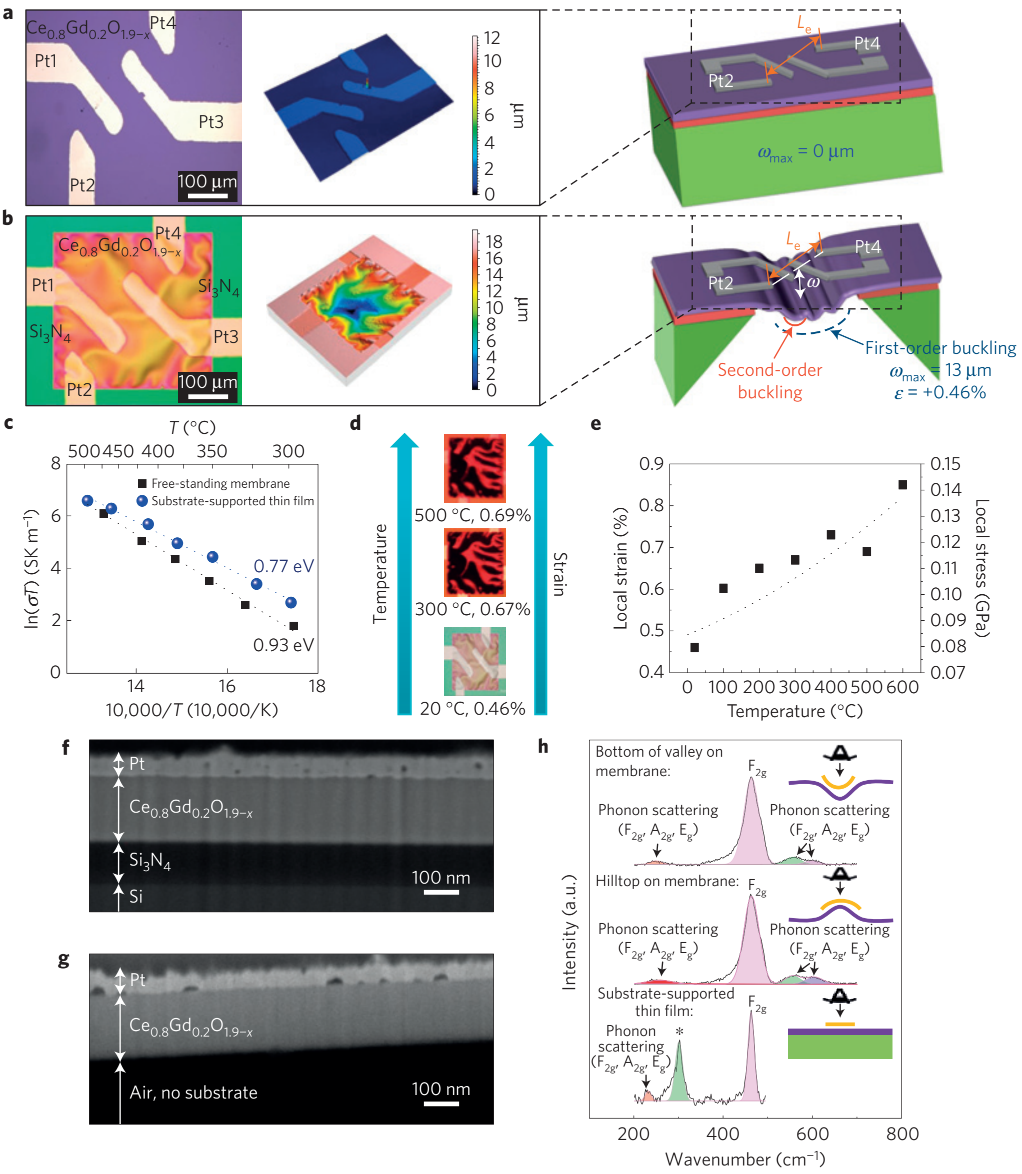

Figure 2 | Probing electro–chemo–mechanics, the tie between oxygen ionic transport–oxygen anionic–cationic near order–strain. a,**b**, Top-view microscopy visuals and three-dimensional profile images from optical profilometry as well as the corresponding schematic cross-sections of the substrate-supported flat and free-standing membrane of $Ce_{0.8}Gd_{0.2}O_{1.9-x}$ thin films with top Pt microelectrodes. **c**, Arrhenius diagram of ionic conductivity for the substrate-supported flat and free-standing membrane of $Ce_{0.8}Gd_{0.2}O_{1.9-x}$ under compressive strain. **d**, *In situ* light microscopy-recorded high-temperature microstructure evolution showing mechanical compression of the $Ce_{0.8}Gd_{0.2}O_{1.9-x}$ membranes during electrical conduction measurements at the respective temperatures indicated. **e**, Evolution of the local maximum mean strain and stress of the free-standing $Ce_{0.8}Gd_{0.2}O_{1.9-x}$ film measured between the electrode-patterned membrane with respect to *in situ* heating in air. **f**,**g**, SEM micrographs of the FIB-cut cross-sections for the substrate-supported $Ce_{0.8}Gd_{0.2}O_{1.9-x}$ films with top Pt microelectrodes on Si_3N_4/Si substrates (**f**) and for the case of a free-standing membrane (**g**). **h**, Atomistic near-order characteristics: micro-Raman spectra of the F_{2g} cationic–oxygen anionic stretching and phonon scatter modes of the $Gd_{0.2}Ce_{0.8}O_{1.9-x}$ films with respect to substrate support and hilltops or valleys of the free-standing membrane.

a single (crystalline) phase with a characteristic thermal expansion coefficient of 1.27×10^{-5} °C^{-1} for 20–600 °C (Supplementary Information 1 and 2). A chip with 16 solid oxygen ion conducting membranes with different microelectrode design and strain alterations is presented in Fig. 1e.

We compare the buckling response and conductivity for an equal set of Pt microelectrode designs located on top of free-standing and substrate-supported $Ce_{0.8}Gd_{0.2}O_{1.9-x}$ thin films (Fig. 2). The microelectrode pattern and flat surface of the $Ce_{0.8}Gd_{0.2}O_{1.9-x}$ film are apparent from the optical and interferometry images of the substrate-supported film (Fig. 2a). For the free-standing $Ce_{0.8}Gd_{0.2}O_{1.9-x}$ film, downward buckling and change in out-of-plane deflection amplitude up to $\omega_{max} = 13\,\mu m$ is found (Fig. 2b). For both films, the lattice structure of the $Ce_{0.8}Gd_{0.2}O_{1.9-x}$ is biaxially compressed: the membrane buckles to reach a new metastable equilibrium with a net compressive strain resulting from intrinsic stresses due to the chosen film growth conditions and also extrinsic ones, that is, thermal expansion mismatch (substrate–film)[13,35,37,38] (Fig. 2b). In Supplementary Information 4, we detail the nomenclature used in the following and exemplify the effect of changing the residual net stress from tensile to compressive for $Ce_{0.8}Gd_{0.2}O_{1.9-x}$ films by initial pulsed laser deposition temperature choice. Only substrate-supported films under residual compressive (in-plane) stress form buckled membranes because tensile stress leads to membrane cracking after substrate removal (Supplementary Fig. 4).

To quantify the biaxial compressive 'net strain' of the membrane $Ce_{0.8}Gd_{0.2}O_{1.9-x}$ films, we analyse their 'first-order maximum strain' measured between the microelectrodes. The buckled membrane can be viewed as a compressed square plate with clamped boundaries attached to the substrate with a critical buckling strain, ε_c, given by equation (1) (ref. 11):

$$\varepsilon_c = -4.365/(1+\nu)(h/L)^2 \qquad (1)$$

where ν is the Poisson ratio, L is the length between the electrodes, and h is the film thickness. For the gadolinia-doped ceria membranes fabricated in this study, a critical buckling strain of $\varepsilon_c = -1.21 \times 10^{-6}$ is calculated, which is a factor of two smaller than yttria-stabilized-zirconia membranes (respectively $\varepsilon_c = -2.1 \times 10^{-6}$; ref. 11). The classic analysis describes the first buckling mode for which the residual buckling strain, ε_r, is larger than the critical strain ($\varepsilon_r > \varepsilon_c$). ε_r can be estimated for the $Ce_{0.8}Gd_{0.2}O_{1.9-x}$ membranes from the maximum out-of-plane deflection amplitude, $\omega_{\max}$, between the inner electrodes, L_e (ref. 39):

$$\varepsilon_r \approx \frac{\sigma_0}{E} \approx \left(\frac{\omega_{\max}}{0.52L_e}\right)^2 \qquad (2)$$

where σ_0 is the residual stress and E is the elastic modulus of the material (for example, 17 GPa for $Ce_{0.8}Gd_{0.2}O_{1.9-x}$; ref. 40). The calculated residual compressive strain of the $Ce_{0.8}Gd_{0.2}O_{1.9-x}$ free-standing membranes increases to 0.46 ± 0.004% ($\omega_{\max} = 13.01 \pm 0.01\,\mu$m and $L_e = 370\,\mu$m) when compared with the flat $Ce_{0.8}Gd_{0.2}O_{1.9-x}$ substrate-supported films ($\omega_{\max} = 0\,\mu$m) at 20 °C (Fig. 2a,b). This is in good agreement with another report of -0.45 ± 0.01% strain for a membrane of comparable geometry and chemical composition but without the application of top microelectrodes[33]. (Further descriptions of strain states and theory are provided in Supplementary Information 4.)

The electric conductivity was investigated to evaluate the role of the residual strain on the $Ce_{0.8}Gd_{0.2}O_{1.9-x}$ membrane by comparing the substrate-supported thin film and free-standing thin film through the microelectrodes (Fig. 2c). The Arrhenius behaviour reveals higher conductivity for the substrate-supported films at low temperatures as compared with the same material as a free-standing buckled membrane. The substrate-supported film had an activation energy of 0.77 ± 0.03 eV, which is in good agreement with literature on $Ce_{0.8}Gd_{0.2}O_{1.9-x}$ pulsed laser deposited films measured by microelectrodes[8,9] and bulk pellets[9,41,42].

The free-standing buckled membrane with a measured residual compressive strain of -0.46 ± 0.004% had an activation energy increase by almost 20% to the value of 0.93 ± 0.03 eV. To the best of our knowledge, this is the first measurement of activation energy changes under strain measured through microelectrode arrangements for free-standing membranes and comparison to literature is not possible. The predominant oxygen ionic nature of the conductivity for the strained $Ce_{0.8}Gd_{0.2}O_{1.9-x}$ membranes is confirmed by oxygen partial pressure-dependent conductivity measurements (Supplementary Information 3). Examples of the electrochemical impedance spectra are presented in Supplementary Information 5.

We experimentally confirm the computational predictions[23] for these real device structures: a hampered oxygen-vacancy migration leading to an increased activation energy for $Ce_{0.8}Gd_{0.2}O_{1.9-x}$ fluorite structures under compressive strain.

Additionally, the $Ce_{0.8}Gd_{0.2}O_{1.9-x}$ films are heated during conductivity measurements demonstrating an increase of compressive strain from -0.46 to -0.85 ± 0.02% for heating from 20 to 600 °C with 5 °C min^{-1} (Fig. 2d,e). The focused ion beam (FIB)-cut scanning electron microscopy (SEM) cross-sections of the Pt microelectrode and $Ce_{0.8}Gd_{0.2}O_{1.9-x}$ film interfaces and substrates are shown after the electric and strain measurements for the substrate-supported samples (Fig. 2f), and free-standing membrane films (Fig. 2g). The cross-sections confirm a good adhesion between the interfaces with no visible alteration after the electric measurements.

Motivated by the observed change in ionic conduction relative to the 'net strain' measured on these materials, we further investigate how this electro–mechanic interaction is correlated with the relative atomistic lattice position changes in the material. It is important to note that the net strain studied refers to the first-order maximum strain measured between the device electrodes. One can additionally observe a smaller amplitude second-order 'waviness' that superimposes the in-plane 'net compressive strain' (Fig. 2b). We turn to micro-Raman spectroscopy to locally resolve the anion–cation near order, by measuring the F_{2g} stretching mode for the substrate-supported and buckled $Ce_{0.8}Gd_{0.2}O_{1.9-x}$ films[43] (Fig. 2h). Here, the incident beam is perpendicular to the surface; that is, the out-of-plane component of the strain shows the biggest contributions. Based on the strain tensor theorems (Supplementary Information 4), conclusions can be drawn for the in-plane strain. We report a characteristic wavenumber of 462.7 cm^{-1} for the F_{2g} cation–oxygen stretching mode for the substrate-supported and flat $Ce_{0.8}Gd_{0.2}O_{1.9-x}$ films. The effective near-order change relative to the direction of buckling, perpendicular to the surface, could successfully be determined for the free-standing membrane by an average net shift of the F_{2g} mode to 464.1 cm^{-1}. We conclude that all free-standing membranes show compressive in-plane strain on an atomistic level compared with the flat substrate-supported film, in agreement with profilometry measurements. The second-order strain alterations are determined by measuring shifts of the F_{2g} Raman mode in the 'hilltops and valleys' that superimpose the overall downward buckled membrane (Fig. 2h). An increase by +0.7 cm^{-1} (red shift) is measured on the bottom of a valley and, in congruence, a decrease of -0.7 cm^{-1} (blue shift) on the hilltop is measured with a spatial resolution of 850 nm for the compressively strained membrane. Literature analysis of a high-pressure study[44] reveals that the shifts by 0.7 cm^{-1} for the free-standing $Ce_{0.8}Gd_{0.2}O_{1.9-x}$ membranes would correspond to an effective compressive strain of ~1.3%. Unlike X-ray diffraction, Raman is a direct measurement of the near-order change by oxygen anion–cation vibrations; we rank it as a significant descriptive characteristic for ionic transport modifications under strain—connecting lattice near-order bond changes to transport and strain.

We can, for the first time, locally resolve the near-order changes in the atomistic position of the fluorite structures for substrate and self-supported membranes of $Ce_{0.8}Gd_{0.2}O_{1.9-x}$ relative to the compressive strain imposed. The experimentally observed shifts in the F_{2g} mode represent the changes in anion–cation near order under strain. This pinpoints the changes in the oxygen ionic migration space around a vacancy and potential shifts in the dopant–host association energies. Both contributions would actively modify the oxygen ion conduction activation energies as reported under compressive strain for the $Ce_{0.8}Gd_{0.2}O_{1.9-x}$ membranes versus flat films in Fig. 2h. (See Supplementary Information 6 for additional Raman data.)

Based on the observation that compressive lattice strain alters the ionic conductivity of a free-standing $Ce_{0.8}Gd_{0.2}O_{1.9-x}$ film when compared with its substrate-supported counterpart, the next question addressed is how various microelectrode geometries on top of the films may be employed to modify the strain between electrodes and subsequently the ionic transport. In Fig. 3a–c, the microelectrode designs a, b and c fabricated on the $Ce_{0.8}Gd_{0.2}O_{1.9-x}$ membranes are compared through optical microscopy, optical profilometry and SEM. The largest buckling is located at the

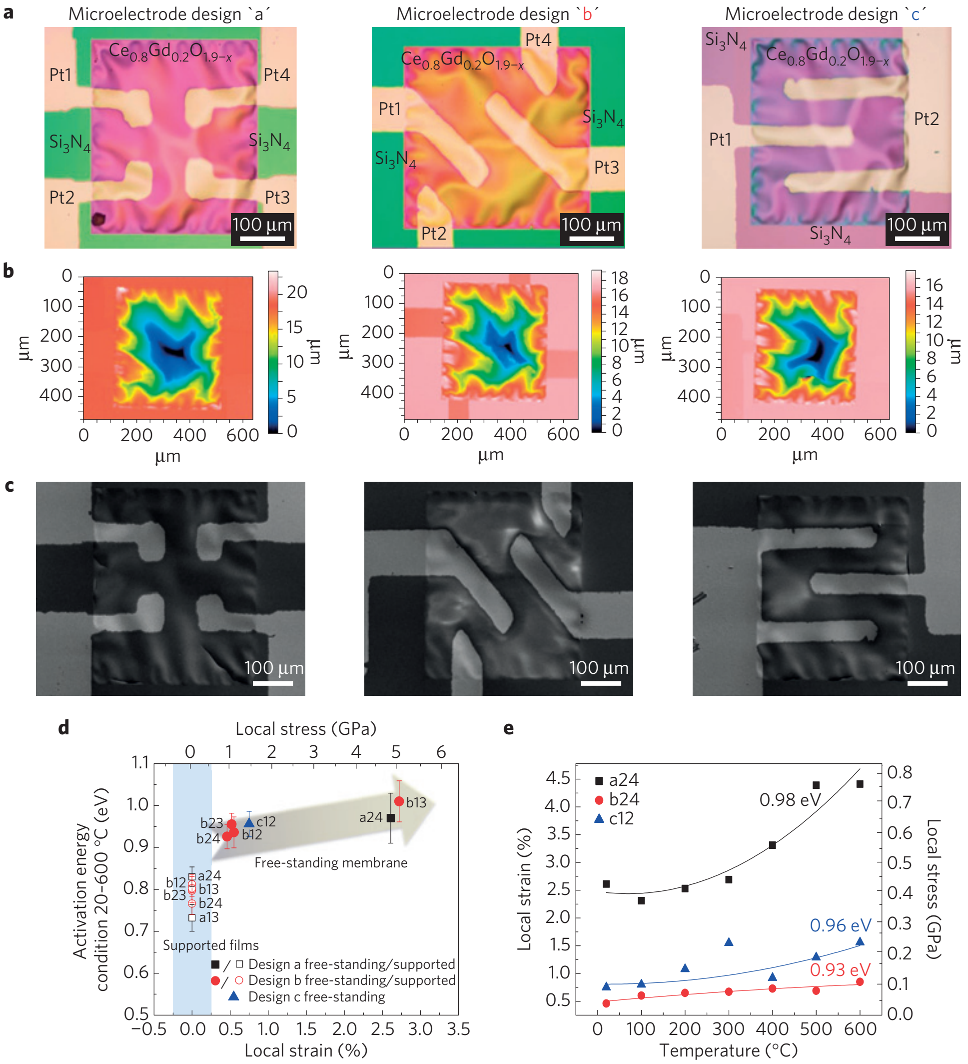

Figure 3 | Microelectrode designs to tune strain patterns of oxygen ionic conducting energy conversion membranes. a, Different Pt microelectrode designs 'a–c' on $Ce_{0.8}Gd_{0.2}O_{1.9-x}$ free-standing membranes. **b**, The optical profilometry illustrates the surfaces of the free-standing membranes with respect to the applied microelectrode design. **c**, Top-view SEM micrographs with respect to the applied microelectrode design. **d**, Comparison of the activation energy of ionic conduction for the self-supported, compressively strained, membranes with various microelectrode designs relative to the same electrode designs measured on supported, flat thin-film structures. The according strain characteristics (and stress) are specified for reference measurements at room temperature based on the maximum out-of-plane amplitude between the electrodes accessed. **e**, *In situ* measured strain (stress) evolution between electrodes with respect to temperature based on maximum out-of-plane amplitude determined between the electrodes.

centre of the membrane independent of microelectrode design. Increasing the distance between the electrodes from 100 µm to 370 µm increases the out-of plane deformation for our model designs such that a > b > c. The design of electrode affects the buckling condition and strain distribution of the $Ce_{0.8}Gd_{0.2}O_{1.9-x}$ membranes. To quantify the implication of net compressive strain on the $Ce_{0.8}Gd_{0.2}O_{1.9-x}$ membranes' ionic conductivity, the activation energies are compared. The ionic conductivity is shown for the different microelectrode design (a to c) and electrodes tested (numbered) for the free-standing and substrate-supported $Ce_{0.8}Gd_{0.2}O_{1.9-x}$ films (Fig. 3d). The activation energy of ionic conductivity of the free-standing membranes does slightly increase with the effective strain measured between the electrodes and can be tuned through the electrode design pattern: the activation energy value increases from 0.93 to 1.01 ± 0.04 eV with increasing compressive strain from −0.46 to −2.70 ± 0.002%. As a proof-of-concept, identical microelectrode design patterns a–c were used for measurements of the flat substrate-supported $Ce_{0.8}Gd_{0.2}O_{1.9-x}$ films. We confirm a mean activation energy of ionic conduction of 0.74 ± 0.03 eV independent of the microelectrode design for zero-strained and flat films, in which 'zero strain' means no strain from deformation of thin film. The corresponding Arrhenius plots are presented in Supplementary Information 7.

The experimental evidence presented for the increased conductivity due to compressive strain supports earlier density functional theory-based calculations of the effect of strain on lattice and oxygen ionic transport in the fluorite structures[22,23]. This effect can be explained by extended formation of vacancy–dopant clusters that have been reported with increasing compressive strain in such structures[9], and changes in the oxygen ionic migration enthalpy that are due to the varied atomistic lattice positions[22,23]. We confirm electro–chemo–mechanic interactions through a combination of near-order cation–oxygen anion analysis by Raman and electric transport measurements relative to strain in $Ce_{0.8}Gd_{0.2}O_{1.9-x}$ model structures and devices.

It is interesting to note that the choice of the microelectrode design pattern alters the effective compressive net strain and therefore can tune the activation energy by up to ~0.27 eV

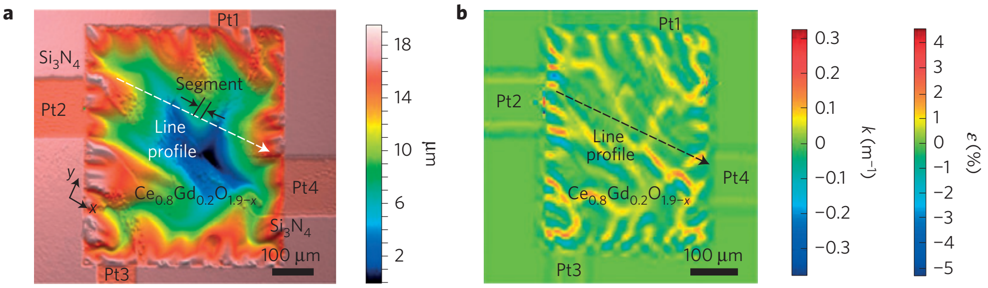

Figure 4 | Computation of second-order buckling strain patterns for oxygen ionic conducting energy conversion membranes. a, Microelectrode design b and local curvature changes in a free-standing ionic conducting $Ce_{0.8}Gd_{0.2}O_{1.9-x}$ electrolyte film integrated on a Si_3N_3/Si wafer as measured by optical profilometry. **b**, The corresponding computed curvature and strain pattern. Here, k denotes the curvature and ε denotes the local strain.

(in-plane); which is of interest for device engineering to actively manipulate the electro–chemo–mechanics beyond classic doping strategies. For such devices, understanding and engineering microelectrode designs to tune the overall net strain but also second-order buckling patterns and local strain distribution of the ionic conductor may be the key to new performances. We exemplify and use the wafer curvature technique to calculate the local strain distribution in the area between the Pt electrodes on the free-standing membrane (Fig. 4). Conventionally, the net stress of the whole membrane is calculated from Stoney's equation[45,46]

$$\sigma = \frac{h_s^2 E_s k}{6(1-\nu_s) h_{\mathrm{GDC}}} \tag{3}$$

where k is curvature, E_s is Young's modulus of the substrate, ν_s is the Poisson ratio of the substrate, h_s is thickness of the Si substrate, and h_{GDC} is the thin-film thickness. Here, it is assumed that the influence of the insulating silicon nitrate layer is negligible compared with the bending moment of the substrate. By assuming elastic deformations, Hooke's law can be used to convert stress in the membrane to strain, that is, $\varepsilon = \sigma / E_{\mathrm{GDC}}$. We exemplify the analysis by the experimental optical profile measurements of a free-standing $Ce_{0.8}Gd_{0.2}O_{1.9-x}$ membrane with top Pt microelectrodes of design b measured at room temperature (Fig. 4a). The in-plane spatial resolution of the optical profilometry measurements is $1.66 \times 1.66\,\mu$m. A strain value, ε, is computed for each pixel (using the parameters: $\nu_s = 0.3$, $h_{\mathrm{GDC}} = 240$ nm, $h_s = 380$ µm, $E_{\mathrm{GDC20}} = 16$ GPa (ref. 47), and $E_s = 165$ GPa (ref. 48)) yielding a strain pattern distribution over the entire membrane as shown in Fig. 4b. We provide the corresponding strain computation code open-source (see Methods for access). It is interesting to note that the effective strains for valleys and hilltops can range from −2% to 2% depending on the locality of the $Ce_{0.8}Gd_{0.2}O_{1.9-x}$ membrane (see also Supplementary Information 8). The optical profilometry measurements agree well with the Raman analysis of the second-order buckling modes and demonstrate the power of both complementary techniques to locally resolve strain patterns in the solid-state membranes relative to microelectrode design.

Thereby, the compressive strain per membrane area can be controlled to keep the atomistic positions in equilibrium, facilitating ionic transport without strong defect clustering and fast migration pathways for energy conversion membranes. This is an important strategy to engineer and twist the electro–chemo–mechanics for energy conversion membranes and thin-film devices based on $Ce_{0.8}Gd_{0.2}O_{1.9-x}$ materials.

Conclusions

This work shows that electro–chemo–mechanics can actively be used to manipulate the cation–oxygen anionic near-order structures through strain to tune the oxygen ionic transport kinetics of ceria-based electrolytes. The model experiments and results presented here demonstrate that the oxygen ionic transport of $Ce_{0.8}Gd_{0.2}O_{1.9-x}$ electrolyte films is affected by mechanical strain and can therefore be substantially altered by the design of Pt microelectrodes. Compressive net strains between electrodes observed by optical profilometry of up to ∼−2.7% can vary the activation energy of ionic conductivity by ∼+0.27 eV for $Ce_{0.8}Gd_{0.2}O_{1.9-x}$ films. We have also developed a code that maps the second-order strain distribution superimposing the first-order strain in the membrane by the wafer curvature technique. The trend for local strain is qualitatively similar to the strain determined from lattice anionic–cationic bond strength changes by Raman spectroscopy, and demonstrates this tool as a strong complementary method for mapping the strain distribution in thin solid films.

The experimental findings on materials of strain–ionic transport alteration rationalize earlier computational reports of defect clustering and reduced ionic migration energy for compressive strain acting on the fluorite structures[22,23]. Furthermore, we demonstrate a proof-of-concept for the manipulation of a material's electro–chemo–mechanic coupling through microelectrode design pattern alterations in realistic micro electrochemical energy conversion devices. The implication of tuning the ionic conductivity of an electrolyte through effective local strains engineered in the membrane is similarly powerful to using classic solid-solution doping of the host lattice. It can be concluded that the power data published for micro solid-oxide fuel cells[1,3] result from strong variations in their electro–chemo–mechanics depending on the mechanical stress forces in the lattice of the ionic conducting electrolytes at equivalent open circuit voltage and temperature conditions.

On the basis of the fundamentals established and the hands-on demonstration through microelectrode model experiments and computations, it can be recognized that the effective 'net strain' on the lattice of the ion conductor membranes directly alters its activation energy and the absolute conductivity between the electrodes of a membrane. It is advisable to keep tensile lattice strains at a maximum for the out-of-plane direction of gadolinia-doped ceria film electrolytes to accelerate the ionic diffusion in future micro electrochemical conversion devices such as fuel cells, electrolysers, and new types of resistive sensor or memristor.

Methods

Methods and any associated references are available in the online version of the paper.

Received 15 September 2014; accepted 26 March 2015;
published online 15 June 2015

References

1. Evans, A., Bieberle-Hütter, A., Rupp, J. L. M. & Gauckler, L. J. Review on microfabricated micro-solid oxide fuel cell membranes. *J. Power Sources* **194,** 119–129 (2009).
2. Evans, A. *et al.* Micro-solid oxide fuel cells: Status, challenges, and chances. *Monatsh. Chem.* **140,** 975–983 (2009).

3. Garbayo, I. *et al.* Full ceramic micro solid oxide fuel cells: Towards more reliable MEMS power generators operating at high temperatures. *Energy Environ. Sci.* **7,** 3617–3629 (2014).
4. Wachsman, E., Ishihara, T. & Kilner, J. Low-temperature solid-oxide fuel cells. *MRS Bull.* **39,** 773–779 (2014).
5. Oudenhoven, J. F. M., Baggetto, L. & Notten, P. H. L. All-solid-state lithium-ion microbatteries: A review of various three-dimensional concepts. *Adv. Energy Mater.* **1,** 10–33 (2011).
6. Waser, R., Dittmann, R., Staikov, G. & Szot, K. Redox-based resistive switching memories - nanoionic mechanisms, prospects, and challenges. *Adv. Mater.* **21,** 2632–2663 (2009).
7. Messerschmitt, F., Kubicek, M., Schweiger, S. & Rupp, J. L. M. Memristor kinetics and diffusion characteristics for mixed anionic-electronic $SrTiO_{3-\delta}$ bits: The memristor-based cottrell analysis connecting material to device performance. *Adv. Funct. Mater.* **24,** 7448–7460 (2014).
8. Rupp, J. L. M. Ionic diffusion as a matter of lattice-strain for electroceramic thin films. *Solid State Ion.* **207,** 1–13 (2012).
9. Rupp, J. L. M. *et al.* Scalable oxygen-ion transport kinetics in metal-oxide films: Impact of thermally induced lattice compaction in acceptor doped ceria films. *Adv. Funct. Mater.* **24,** 1562–1574 (2014).
10. Rupp, J. L. M., Scherrer, B., Schäuble, N. & Gauckler, L. J. Time-temperature-transformation (TTT) diagrams for crystallization of metal oxide thin films. *Adv. Funct. Mater.* **20,** 2807–2814 (2010).
11. Evans, A. *et al.* Residual stress and buckling patterns of free-standing yttria-stabilized-zirconia membranes fabricated by pulsed laser deposition. *Fuel Cells* **12,** 614–623 (2012).
12. Kerman, K., Xuza, S. & Ramanathan, S. Free standing yttria-doped zirconia membranes: Geometrical effects on stability. *J. Electroceramics* **34,** 91–99 (2015).
13. Tuller, H. L. & Bishop, S. R. Point defects in oxides: Tailoring materials through defect engineering. *Annu. Rev. Mater. Res.* **41,** 369–398 (2011).
14. Yildiz, B. "Stretching" the energy landscape of oxides—effects on electrocatalysis and diffusion. *MRS Bull.* **39,** 147–156 (2014).
15. Schweiger, S., Kubicek, M., Messerschmitt, F., Murer, C. & Rupp, J. L. M. A micro-dot multilayer oxide device: Let's tune the strain-ionic transport interaction. *ACS Nano* **8,** 5032–5048 (2014).
16. Schichtel, N., Korte, C., Hesse, D. & Janek, J. Elastic strain at interfaces and its influence on ionic conductivity in nanoscaled solid electrolyte thin films—theoretical considerations and experimental studies. *Phys. Chem. Chem. Phys.* **11,** 3043–3048 (2009).
17. Tsvetkov, N., Lu, Q., Chen, Y. & Yildiz, B. Accelerated oxygen exchange kinetics on $Nd_2NiO_{4+\delta}$ thin films with tensile strain along c-axis. *ACS Nano* **9,** 1613–1621 (2015).
18. Sillassen, M. *et al.* Low-temperature superionic conductivity in strained yttria-stabilized zirconia. *Adv. Funct. Mater.* **20,** 2071–2076 (2010).
19. MohanKant, K., Esposito, V. & Pryds, N. Strain induced ionic conductivity enhancement in epitaxial $Ce_{0.9}Gd_{0.1}O_{2-\delta}$ thin films. *Appl. Phys. Lett.* **100,** 033105 (2012).
20. Garcia-Barriocanal, J. *et al.* Colossal ionic conductivity at interfaces of epitaxial ZrO_2:Y_2O_3/$SrTiO_3$ heterostructures. *Science* **321,** 676–680 (2008).
21. Korte, C. *et al.* Coherency strain and its effect on ionic conductivity and diffusion in solid electrolytes—an improved model for nanocrystalline thin films and a review of experimental data. *Phys. Chem. Chem. Phys.* **16,** 24575–24591 (2014).
22. Hinterberg, J., Zacherle, T. & De Souza, R. A. Activation volume tensor for oxygen-vacancy migration in strained CeO_2 electrolytes. *Phys. Rev. Lett.* **110,** 205901 (2013).
23. De Souza, R. A., Ramadan, A. & Hörner, S. Modifying the barriers for oxygen-vacancy migration in fluorite-structured CeO_2 electrolytes through strain: A computer simulation study. *Energy Environ. Sci* **5,** 5445–5453 (2012).
24. Shen, W., Jiang, J. & Hertz, J. L. Reduced ionic conductivity in biaxially compressed ceria. *RSC Adv.* **4,** 21625–21630 (2014).
25. Schichtel, N. *et al.* On the influence of strain on ion transport: Microstructure and ionic conductivity of nanoscale YSZ|Sc_2O_3 multilayers. *Phys. Chem. Chem. Phys.* **12,** 14596–14608 (2010).
26. Shen, W., Jiang, J. & Hertz, J. L. Beneficial lattice strain in heterogeneously doped ceria. *J. Phys. Chem. C* **118,** 22904–22912 (2014).
27. Huang, H. *et al.* High-performance ultrathin solid oxide fuel cells for low-temperature operation. *J. Electrochem. Soc.* **154,** B20–B24 (2007).
28. Bieberle-Hütter, A., Reinhard, P., Rupp, J. L. M. & Gauckler, L. J. The impact of etching during microfabrication on the microstructure and the electrical conductivity of gadolinia-doped ceria thin films. *J. Power Sources* **196,** 6070–6078 (2011).
29. Rupp, J. L. M., Muecke, U. P., Nalam, P. C. & Gauckler, L. J. Wet-etching of precipitation-based thin film microstructures for micro-solid oxide fuel cells. *J. Power Sources* **195,** 2669–2676 (2010).
30. Kerman, K., Tallinen, T., Ramanathan, S. & Mahadevan, L. Elastic configurations of self-supported oxide membranes for fuel cells. *J. Power Sources* **222,** 359–366 (2013).
31. Garbayo, I. *et al.* Electrical characterization of thermomechanically stable YSZ membranes for micro solid oxide fuel cells applications. *Solid State Ion.* **181,** 322–331 (2010).
32. Safa, Y., Hocker, T., Prestat, M. & Evans, A. Post-buckling design of thin-film electrolytes in micro-solid oxide fuel cells. *J. Power Sources* **250,** 332–342 (2014).
33. Greenberg, B. M., Wachtel, E., Lubomirsky, I., Fleig, J. & Maier, J. Elasticity of solids with a large concentration of point defects. *Adv. Funct. Mater.* **16,** 48–52 (2006).
34. Lubomirsky, I. Stress adaptation in ceramic thin films. *Phys. Chem. Chem. Phys.* **9,** 3701–3710 (2007).
35. Lubomirsky, I. Practical applications of the chemical strain effect in ionic and mixed conductors. *Monatsh. Chem.* **140,** 1025–1030 (2009).
36. Marrocchelli, D., Bishop, S. R., Tuller, H. L. & Yildiz, B. Understanding chemical expansion in non-stoichiometric oxides: Ceria and zirconia case studies. *Adv. Funct. Mater.* **22,** 1958–1965 (2012).
37. Davis, L. *Investigation of Residual and Thermal Stress on Membrane-Based MEMS Devices* (Univ. South Florida, 2009); http://scholarcommons.usf.edu/etd/1925
38. Baertsch, C. *et al.* Fabrication and structural characterization of self-supporting electrolyte membranes for a micro solid-oxide fuel cell. *J. Mater. Res.* **19,** 2604–2615 (2004).
39. Timoshenko, S. P. *Theory of Elastic Stability* (Dover, 2009).
40. Kossoy, A. *et al.* Influence of point-defect reaction kinetics on the lattice parameter of $Ce_{0.8}Gd_{0.2}O_{1.9}$. *Adv. Funct. Mater.* **19,** 634–641 (2009).
41. Anjaneya, K. C., Nayaka, G. P., Manjanna, J., Govindaraj, G. & Ganesha, K. N. Preparation and characterization of $Ce_{1-x}Gd_xO_{2-\delta}$ ($x = 0.1$–0.3) as solid electrolyte for intermediate temperature SOFC. *J. Alloys Compd.* **578,** 53–59 (2013).
42. Mogensen, M., Sammes, N. & Tompsett, G. Physical, chemical and electrochemical properties of pure and doped ceria. *Solid State Ion.* **129,** 63–94 (2000).
43. Giannici, F. *et al.* Structure and oxide ion conductivity: Local order, defect interactions and grain boundary effects in acceptor-doped ceria. *Chem. Mater.* **26,** 5994–6006 (2014).
44. Kourouklis, G. A., Jayaraman, A. & Espinosa, G. P. High-pressure Raman study of CeO_2 to 35 GPa and pressure-induced phase transformation from the fluorite structure. *Phys. Rev. B* **37,** 4250–4253 (1988).
45. Stoney, G. G. The tension of metallic films deposited by electrolysis. *Proc. R. Soc. Lond. A* **82,** 172–175 (1909).
46. Feng, X., Huang, Y. & Rosakis, A. J. On the Stoney formula for a thin film/substrate system with nonuniform substrate thickness. *J. Appl. Mech.* **74,** 1276–1281 (2007).
47. Yasuda, K., Uemura, K. & Shiota, T. Sintering and mechanical properties of gadolinium-doped ceria ceramics. *J. Phys. Conf. Ser.* **339,** 012006 (2012).
48. Dolbow, J. & Gosz, M. Effect of out-of-plane properties of a polyimide film on the stress fields in microelectronic structures. *Mech. Mater.* **23,** 311–321 (1996).

Acknowledgements

S. Li is thanked for support in carrying out parts of the electric measurements. N. Spencer, C. Crémmel, C. Schneider and T. Lippert are thanked for their assistance with analytical tools. The authors acknowledge P. Muralt for providing the Si_3N_4-coated Si wafers as substrate samples. M. Kubicek, M. Struzik, M. Rawlence and Z. Lapin are thanked for discussion and proof reading. This work was supported by the Swiss National Science Foundation under the project numbers of 144988, 147190 and 138914.

Author contributions

Y.S. and S.S. performed and executed the experiments and J.L.M.R. discussed and supervised the work. A.H.B. carried out the computational analysis in collaboration with J.L.M.R. and Y.S. The paper was co-written by Y.S., A.H.B., S.S. and J.L.M.R., and all authors discussed the results and interpretations, and commented on the manuscript.

Additional information

Supplementary information is available in the online version of the paper. Reprints and permissions information is available online at www.nature.com/reprints. The code that is used to compute the strain state changes can be downloaded open source at http://www.electrochem.mat.ethz.ch/opensource/index. Correspondence and requests for materials should be addressed to J.L.M.R.

Competing financial interests

The authors declare no competing financial interests.

Methods

Material synthesis. $Ce_{0.8}Gd_{0.2}O_{1.9-x}$ ceramic targets were synthesized and sintered: $Ce_{0.8}Gd_{0.2}O_{1.9-x}$ powders (Sigma-Aldrich) were pressed uniaxially and isostatically at 440 bar for 2 min to form a pellet. The pellet was heated to 1,400 °C at 3 °C min^{-1}, sintered for 4 h, and then cooled at 5 °C min^{-1} to room temperature.

The substrates used were, in all cases, double-side-coated 200 nm thin low-stress Si_3N_4-coated silicon wafers with a (100) wafer orientation (4-inch wafer, 380 µm thick). The Si_3N_4 was deposited by low-pressure chemical vapour deposition (Ceramics Laboratory, EPFL).

Pulsed laser deposition (Surface Technologies) was used to deposit thin films on the wafers using the synthesized targets with a KrF excimer laser with a wavelength of 248 nm at an energy of 40 mJ per pulse and a frequency of 10 Hz. The effective spot size was 6 mm^2. After reaching the background pressure of 4×10^{-5} mbar, the thin film was deposited at 400 °C and 0.0267 mbar O_2 pressure. By this recipe 240 ± 10 nm $Ce_{0.8}Gd_{0.2}O_{1.9-x}$ thin films were obtained after 22,000 pulses. This thickness was used for all sample depositions on Si_3N_4-coated silicon chips.

Microfabrication of thin-film membranes. In a first step, the Si_3N_4-coated silicon chips were patterned on one side by photolithography to define the membrane areas with the photoresist ma-N 1420. Following development, the exposed portion of the Si_3N_4 was removed by reactive ion etching (Oxford Instruments RIE 80+). After removing the remaining photoresist by acetone, the wafer was exposed to a KOH (20% w/w) solution at 90 °C for 7 h, whereby free-standing Si_3N_4 membranes were formed. In the second step, pulsed laser deposition was employed to deposit the $Ce_{0.8}Gd_{0.2}O_{1.9-x}$ thin films onto the Si_3N_4 membranes. Subsequently, the Si_3N_4 layers were removed and free-etched at the targeted $Ce_{0.8}Gd_{0.2}O_{1.9-x}$ membrane areas by a second reactive ion etching step. We detail the microfabrication of the membranes in Supplementary Information 9.

Strain, microstructure and structural characterization. In the experiments, the surface profiles of the buckling membrane and flat films were obtained by an optical profilometer (Sensofar, Schaefer-Tec AG). *In situ* heating experiments were carried out with a special heating stage (Linkam PS 92 and PS 1500 systems) up to temperatures of 600 °C.

To identify the $Ce_{0.8}Gd_{0.2}O_{1.9-x}$ phases, *in situ* heated X-ray diffraction patterns (Bruker D8) were measured using Cu Kα radiation and a stepped heating rate of 5 °C min^{-1} between patterns, with each taken at a constant temperature.

Micro-Raman spectroscopy spectra (WITec CRM200) were acquired by a high-resolution microscope, equipped with a 532 nm wavelength excitation laser and a spectral resolution of 0.7 cm^{-1}.

Microstructure cross-sections were investigated for the substrate-supported and free-standing $Ce_{0.8}Gd_{0.2}O_{1.9-x}$ membranes by a FIB scanning electron microscope (Zeiss NVision 40). The gallium beam-induced deposition of the C protection layer and then subsequent milling were carried out at 30 kV and 300 pA. Scanning electron microscopy (SEM, LEO 1530) was used to analyse the surface tomography of the substrate-supported and free-standing membranes at 3 kV. A Dektak surface step profiler (Dektak XT Advanced, Bruker) was used to test the reproducibility of the growth recipe and control possible deviations of the film thickness from the design parameters.

Microelectrode processing and electrical characterization. The microelectrodes were deposited by electron beam evaporation (Physical Vapour Deposition, Evaporation Plassys II) through a shadow mask, resulting in film a thickness of 100 nm, detailed in Supplementary Information 9.

Electrical characterization was performed in a custom-engineered microprobe station (Electrochemical Materials ETH Zurich Switzerland and Everbeing Taiwan) equipped with a hotplate for controlled heating up to 550 °C, a camera for *in situ* microscopy and videography, electrically shielded micromanipulators suitable for electrochemical impedance and temperature positioners, and a closed and controllable atmosphere with gas flow control. Electrical characterization was carried out with a Keithley 6517B with an applied d.c. voltage amplitude of 5 mV. Additionally, electrochemical impedance spectroscopy (Gamry Reference 600) at 200 mV and over a frequency range from 1 Hz to 1 MHz was used. The electrolyte and electrode responses were separated by using a d.c. bias up to 3 V as detailed in Supplementary Information 5. Temperature was measured with K-type thermocouples mounted on micromanipulators and a Keithley 2601B. A part of the steering and computing software is offered open-source in http://www.electrochem.mat.ethz.ch/opensource/index.

Computation of strain distribution in a free-standing membrane. We developed a program in MATLAB to compute, from the optical profilometry data of the free-standing membranes, the local strains based on a wafer curvature technique. The strain, ε, in each pixel is the sum of the strain components in the x and y directions. First, the data are smoothed with the MATLAB built-in local regression function SMOOTH with the method LOESS and a span of 10%, which provides a smooth curve with a least-squares quadratic fit. Second, the curvature is determined by the second-order derivative of the smooth curve. A curvature value is thus assigned to each element and the stress or strain can be determined by Stoney's equation (see equation (3)). We provide the corresponding strain computation as open-source code at http://www.electrochem.mat.ethz.ch/opensource/index.